MATERIALS SCIENCE

Anomalous absorption of electromagnetic waves by 2D transition metal carbonitride Ti_3CNT_x (MXene)

Aamir Iqbal[1,2,3], Faisal Shahzad[1]*, Kanit Hantanasirisakul[3], Myung-Ki Kim[4], Jisung Kwon[4], Junpyo Hong[1], Hyerim Kim[1,4], Daesin Kim[1,4], Yury Gogotsi[3]†, Chong Min Koo[1,2,4]†

Lightweight, ultrathin, and flexible electromagnetic interference (EMI) shielding materials are needed to protect electronic circuits and portable telecommunication devices and to eliminate cross-talk between devices and device components. Here, we show that a two-dimensional (2D) transition metal carbonitride, Ti_3CNT_x MXene, with a moderate electrical conductivity, provides a higher shielding effectiveness compared with more conductive $Ti_3C_2T_x$ or metal foils of the same thickness. This exceptional shielding performance of Ti_3CNT_x was achieved by thermal annealing and is attributed to an anomalously high absorption of electromagnetic waves in its layered, metamaterial-like structure. These results provide guidance for designing advanced EMI shielding materials but also highlight the need for exploring fundamental mechanisms behind interaction of electromagnetic waves with 2D materials.

The rapid advancement in telecommunication and the ever-increasing number of compact mobile electronic devices and gadgets have caused some serious electromagnetic interference (EMI) issues, including data loss, data misinterpretation, and even system failure caused by strong electromagnetic induction effects in a close proximity (*1*–*6*). It may even affect human health (*4*). Commercialization of emerging highly integrated fifth-generation (5G) wireless devices demands EMI shielding materials with easy processability, light weight, and minimal thickness, along with improved shielding effectiveness (SE) (*7*). Generally, efficient EMI shielding materials are the ones with a high electrical conductivity. However, the most commonly used conducting and nonmagnetic shielding materials, such as metals and carbon-based nanomaterials, including graphene and carbon nanotubes, barely meet these requirements (*1*, *8*–*10*).

Recently, the outstanding EMI shielding properties of $Ti_3C_2T_x$ MXene and its composites have been shown, offering an EMI SE of 92 dB at a thickness of 45 μm in the X-band frequency range (8.2 to 12.4 GHz), showing exceptional promise for applications in advanced smart electronics (*1*). This shielding performance was attributed to the intrinsic electrical conductivity (σ ~4500 S cm^{-1}), abundant surface terminations, and the laminate architecture of $Ti_3C_2T_x$ MXene films, which was later supported by theoretical calculations by Li *et al.* (*11*).

This finding led to exploration of MXenes and their composites and hybrids with other nanomaterials in different structural forms, such as porous foams and aerogels, mechanically strong hybrids, and segregated structures, to further improve the intrinsic EMI shielding properties of MXenes (*4*, *12*–*15*). However, even though control over reflection versus absorption has been demonstrated (*14*), no substantial improvement in total EMI SE has been achieved. Because $Ti_3C_2T_x$ films have shown the highest conductivity among all the MXenes studied so far (*2*, *16*), it was assumed that they offer the best shielding properties.

We report on the EMI shielding ability of a transition metal carbonitride, Ti_3CNT_x MXene, which has a very similar structure to $Ti_3C_2T_x$, with the nitrogen atoms randomly substituting carbon atoms and structurally packed in a hexagonal structure with Ti layers, as shown schematically in Fig. 1A (*17*, *18*). It was initially assumed that the electronic conductivity [free electrons in two-dimensional (2D) sheets of MXene] determines the EMI SE, as is known for bulk metals. As-synthesized Ti_3CNT_x, with a lower electrical conductivity, has a lower EMI SE than $Ti_3C_2T_x$. However, after heat treatment at 350°C, a 40-μm-thick Ti_3CNT_x film showed an EMI SE of 116 dB due to the anomalously high absorption of EM waves in the layered structure, which is larger than the 93 dB measured for annealed $Ti_3C_2T_x$ films of comparable thickness. Moreover, Ti_3CNT_x outperforms all other shielding materials with similar thickness studied to date, including copper, which has several orders of magnitude higher conductivity.

Ti_3CNT_x and $Ti_3C_2T_x$ MXenes were synthesized by chemical etching of the Al atoms from their parent MAX phases, Ti_3AlCN and Ti_3AlC_2, respectively. X-ray diffraction (XRD) patterns of the MAX phases [where M, A, and X stand for transition metal (Ti), aluminum, and carbon or nitrogen, respectively] and the corresponding MXenes are shown in Fig. 1B. Ti_3AlC_2 is a single-phase M_3AX_2 (*19*), whereas the Ti_3AlCN contains traces of the M_4AX_3 and M_2AX phases, which were below detection limit after etching and delamination (*17*). The characteristic (002) peak shifted toward the lower angle with the absence of nonbasal plane peaks of the MAX phases, confirming their complete etching and delamination to Ti_3CNT_x and $Ti_3C_2T_x$ MXenes (*17*, *19*). Fig. S1 shows a transmission electron microscopy (TEM) image of a monolayer Ti_3CNT_x flake with the selected area electron diffraction (SAED) pattern in the inset. The results confirmed that the 2D flake retained the crystallinity and hexagonal structure of the carbonitride layers (*17*).

Ti_3CNT_x and $Ti_3C_2T_x$ free-standing films of different thicknesses were fabricated by vacuum-assisted filtration of their aqueous suspensions, followed by annealing for 6 hours at different temperatures (150°C, 250°C, and 350°C) under an argon atmosphere. Structural changes in Ti_3CNT_x and $Ti_3C_2T_x$ MXene films under thermal annealing were analyzed by XRD, as shown in Fig. 1C and fig. S2, respectively. The (002) peak of the Ti_3CNT_x gradually shifts from 5.76° for the as-synthesized film to higher angles of 6.3°, 6.76°, and 7.1° for the films annealed at 150°C, 250°C, and 350°C, respectively, indicating that the interlayer (*d*-) spacing decreases from 1.53 to 1.40, 1.31, and 1.24 nm, respectively, with increasing temperature. $Ti_3C_2T_x$ also shows similar changes in the *d*-spacing on annealing. However, the *d*-spacing for the Ti_3CNT_x MXene film remains larger than that of $Ti_3C_2T_x$ at the same annealing temperature (fig. S3). The decrement in *d*-spacing is due to the removal of intercalated water and hydroxyl surface terminations at elevated temperatures (*17*). Even though the *d*-spacing decreased with increasing annealing temperature, the pore size and pore volume gradually increased with temperature. Additionally, unlike $Ti_3C_2T_x$, Ti_3CNT_x films reveal a small TiO_2 peak of (101) plane after annealing at 350°C, indicating partial surface oxidation (*20*). Further increase in temperature resulted in much more severe oxidation, deteriorating the properties of Ti_3CNT_x films.

Fig. 1D and fig. S4 show the thermogravimetric analysis–mass spectroscopy (TGA-MS) results of Ti_3CNT_x and $Ti_3C_2T_x$ MXenes, respectively. Ti_3CNT_x and $Ti_3C_2T_x$ exhibit a strong and broad peak at a mass-to-charge ratio (*m*/*z*) of 18 caused by the removal of absorbed water, and a strong peak at a *m*/*z* value of 17, representing the removal of the hydroxyl ion

[1]Materials Architecturing Research Centre, Korea Institute of Science and Technology (KIST), Seoul 02792, Korea. [2]Division of Nano & Information Technology, KIST School, University of Science and Technology, Seoul 02792, Republic of Korea. [3]Department of Materials Science and Engineering and A. J. Drexel Nanomaterials Institute, Drexel University, Philadelphia, PA 19104, USA. [4]KU-KIST Graduate School of Converging Science and Technology, Korea University, Seoul 02841, Korea.
*Present address: National Center for Nanotechnology, Department of Metallurgy and Materials Engineering, Pakistan Institute of Engineering and Applied Sciences (PIEAS), Islamabad 45650, Pakistan.
†Corresponding author. Email: gogotsi@drexel.edu (Y.G.); koo@kist.re.kr (C.M.K.)

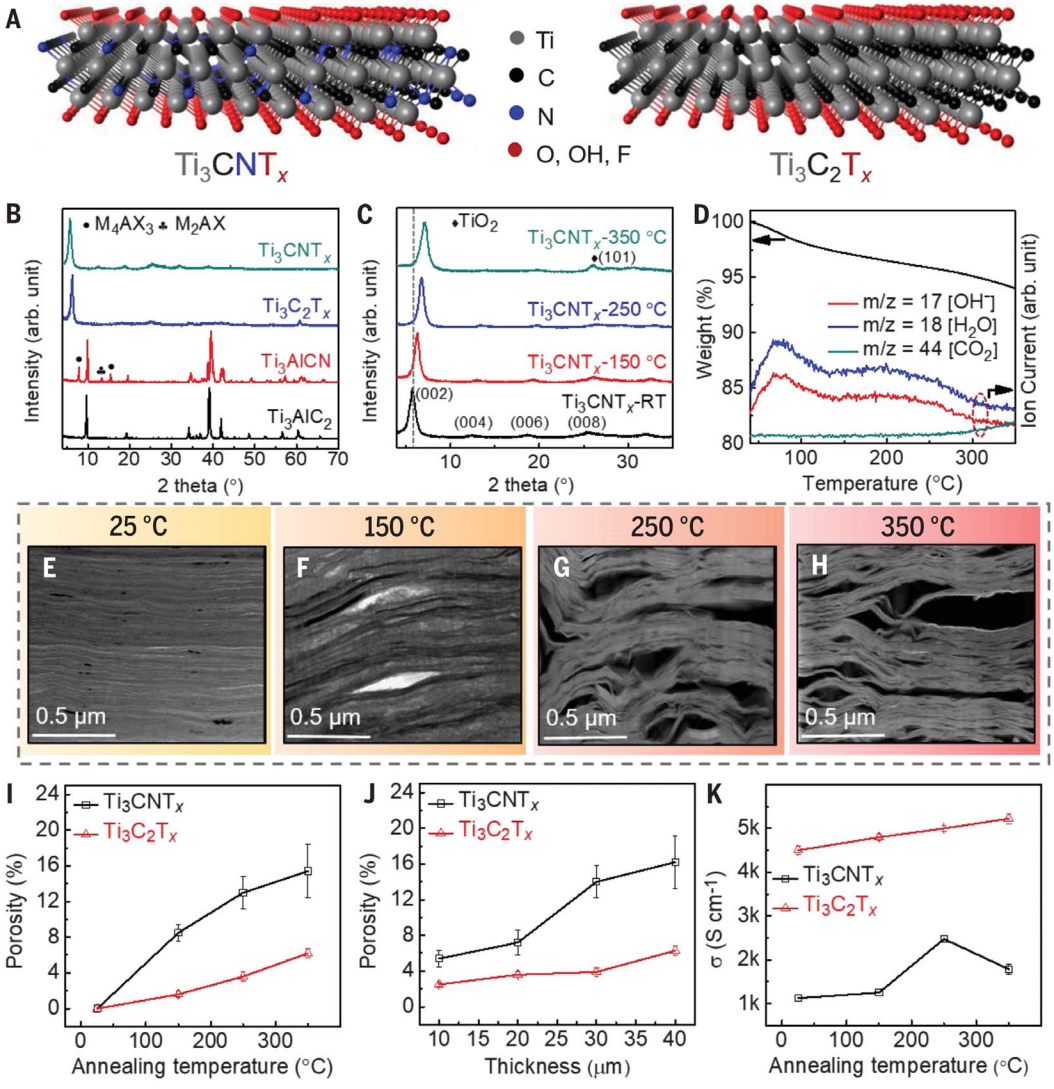

Fig. 1. Morphology, structural and fundamental characterizations. (**A**) Schematic representation of the Ti_3CNT_x and $Ti_3C_2T_x$ MXenes. T_x represents surface terminations (–OH, –O, and –F). (**B**) XRD patterns of Ti_3AlCN and Ti_3AlC_2 MAX and their corresponding MXenes (Ti_3CNT_x and $Ti_3C_2T_x$, respectively). (**C**) XRD patterns of Ti_3CNT_x films annealed at different temperatures. (**D**) TGA-MS thermogram of the Ti_3CNT_x MXene. (**E** to **H**) Cross-sectional TEM images of Ti_3CNT_x films at different annealing temperatures. (**I** and **J**) Comparison of porosity introduced in annealed Ti_3CNT_x and $Ti_3C_2T_x$ MXenes as a function of annealing temperature (I) and the films' initial thickness (J). (**K**) Comparison of electrical conductivity of Ti_3CNT_x and $Ti_3C_2T_x$ as a function of annealing temperature.

(*17*). The results indicate that the as-synthesized Ti_3CNT_x exhibits a larger weight loss of ~6% compared with only ~2% in $Ti_3C_2T_x$, indicating that Ti_3CNT_x holds a larger content of water compared with $Ti_3C_2T_x$ (*17*). Unlike $Ti_3C_2T_x$, Ti_3CNT_x reveals a small signal of m/z = 44, attributed to the evolution of CO_2 above 300°C, indicating that Ti_3CNT_x is less resistive to oxidation than $Ti_3C_2T_x$ at higher temperatures (see the TEM images with SAED patterns of annealed Ti_3CNT_x and $Ti_3C_2T_x$ MXenes in figs. S5 and S6).

Cross-sectional high-resolution TEM (HRTEM) images and scanning electron microscopy (SEM) images show structural changes in 40-μm-thick Ti_3CNT_x films as a function of annealing temperature (Fig. 1, E to H, and fig. S7). The as-synthesized Ti_3CNT_x film shows a compact and well-aligned laminate morphology. By contrast, slit pores were developed in the annealed films with a broad size distribution ranging from tens of nanometers to micrometers. The pore size and pore volume rapidly increase with the annealing temperature. $Ti_3C_2T_x$ also exhibits similar pore generation behavior in the annealed samples (fig. S8), but the pore size and pore volume are much smaller at the same temperature. At the film thickness of 40 μm, the porosity increases with annealing temperature, and this effect is much larger in the case of Ti_3CNT_x films compared with $Ti_3C_2T_x$ (Fig. 1I). The pores are mainly generated by the loss of intercalated water and the loosely adsorbed molecules on the surface, as well as the hydroxyl terminal groups for both Ti_3CNT_x and $Ti_3C_2T_x$. The larger pore size and porosity of Ti_3CNT_x films are due to the larger amount of intercalated water compared with $Ti_3C_2T_x$ films under the same conditions, as suggested by the TGA-MS results (Fig. 1D and fig. S4). The porosity also depends on the initial thickness of the films annealed at fixed temperature of 350°C, as shown in Fig. 1J and fig. S9. The larger porosity in thicker film is attributed to the fact that larger amounts of gaseous compounds generated during heat treatment are entrapped in the film because of difficulty in escaping from the thick and compact laminate structure, resulting in the creation of larger pores and localized ruptures in the thicker laminates. The annealed Ti_3CNT_x films retain superior dimensional stability, good adhesion to the glass substrate, and enough flexibility for potential applications in flexible portable electronics (fig. S10).

X-ray photoelectron spectroscopy (XPS) survey spectra before thermal annealing (fig. S11A) exhibit an N 1*s* peak (~400 eV) in addition to the peaks for the Ti, C, F, O, and Cl elements, which originates from the nitrogen atoms of Ti_3CNT_x with surface terminations. On the other hand, fig. S11B shows the absence of nitrogen in $Ti_3C_2T_x$ (*21*). High-resolution XPS spectra of Ti 2*p* and O 1*s* of Ti_3CNT_x annealed at different temperatures revealed that the Ti-OH content decreases with increasing the annealing temperature up to 300°C, but a further increase in temperature initiates surface oxidation, resulting in the growth of TiO_2 nanocrystals at 350°C (fig. S12, A and B) (*22*). By

contrast, $Ti_3C_2T_x$ films did not show the formation of TiO_2 crystals under identical annealing conditions (fig. S13). These results are in good agreement with XRD and TEM analyses.

Fig. 1K shows the electrical conductivity of Ti_3CNT_x and $Ti_3C_2T_x$ MXene films before and after annealing. The as-synthesized Ti_3CNT_x has an average electrical conductivity of 1125 S cm^{-1}, which gradually increases with annealing temperature and reaches a maximum value of 2475 S cm^{-1} at 250°C, 120% higher than that of the as-synthesized films. This increase in electrical conductivity is due to the removal of intercalated water and other molecules leading to the reduction in interlayer spacing in the annealed samples. The reduced *d*-spacing decreases the interflake resistance between MXene sheets to facilitate electron conduction (*23*). A further increase in annealing temperature results in some decrease in conductivity to 1786 S cm^{-1} at 350°C primarily because of increasing pore volume (*12*). The cross-sectional TEM image of annealed Ti_3CNT_x film at 350°C, coupled with energy-dispersive X-ray spectroscopy (EDS) mapping (fig. S14A), reveals that oxidation occurred only in a very thin surface layer and should have a little effect on the electrical conductivity measurements. The corresponding HRTEM image of the surface part of the film depicts a lattice *d*-spacing of 0.352 nm assigned to the (101) plane of anatase TiO_2 (*24*) (fig. S14B), whereas the inner part of the film (fig. S14C) shows no oxidation and sustains the layered morphology with a *d*-spacing value of 1.21 nm, which is consistent with the XRD data in Fig. 1C. By contrast, $Ti_3C_2T_x$ films showed a monotonous increment in electrical conductivity from 4500 to 5225 S cm^{-1} with increasing annealing temperature, indicating that they are more stable and develop less porosity compared with Ti_3CNT_x films.

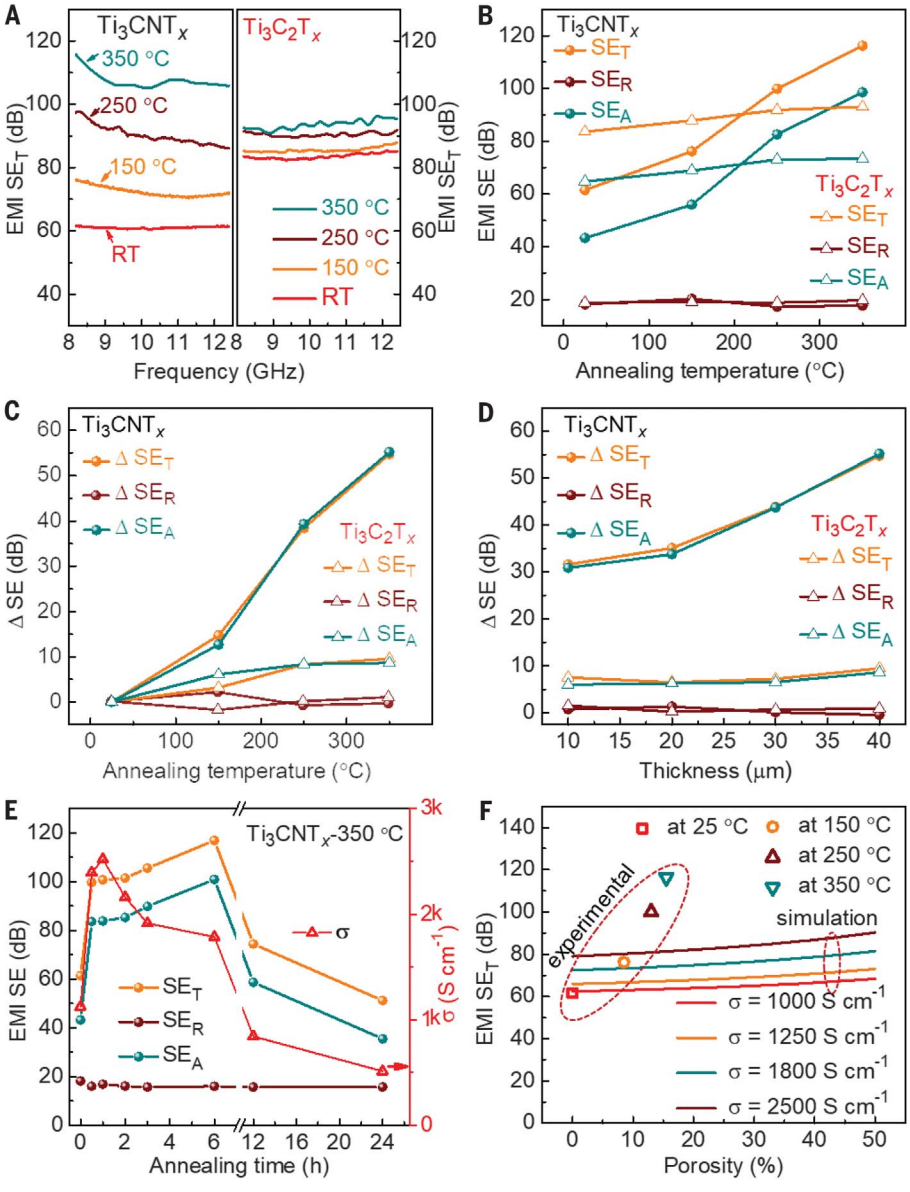

Fig. 2. EMI shielding measurements of Ti_3CNT_x and $Ti_3C_2T_x$ films. (**A**) SE_T of 40-μm Ti_3CNT_x and $Ti_3C_2T_x$ films annealed at different temperatures. (**B**) Comparison of EMI SE_T, SE_R, and SE_A of 40-μm Ti_3CNT_x and $Ti_3C_2T_x$ films annealed at different temperatures. Comparison of ΔSE_T, ΔSE_R, and ΔSE_A of Ti_3CNT_x and $Ti_3C_2T_x$ of (**C**) 40-μm films annealed at different temperatures and (**D**) films with different thicknesses annealed at 350°C. (**E**) Absolute EMI SE_T, SE_R, and SE_A, and electrical conductivity of 40-μm Ti_3CNT_x films annealed at 350°C for different annealing times. (**F**) Comparison of experimental (closed symbols) and theoretical (solid lines) EMI SE_T values. Each color represents corresponding electrical conductivity at the given temperature. Absolute EMI SE_T, SE_R, and SE_A values were taken at 8.2-GHz frequency.

Fig. 2A shows the total EMI SE (SE_T) of 40-μm-thick Ti_3CNT_x and $Ti_3C_2T_x$ films in the X-band frequency range after annealing at various temperatures. SE values caused by reflection (SE_R) and absorption (SE_A) for both MXenes are provided in fig. S15. The as-synthesized Ti_3CNT_x film without heat treatment shows an SE_T of 61 dB, which rises substantially to 77, 99, and 116 dB at annealing temperatures of 150°C, 250°C, and 350°C, respectively. The as-synthesized $Ti_3C_2T_x$ reveals an SE_T of 84 dB, which gradually rises to 87, 92, and 93 dB after annealing at 150°C, 250°C, and 350°C, respectively. Fig. 2B summarizes the absolute SE_T, SE_R, and SE_A values for 40-μm-thick Ti_3CNT_x and $Ti_3C_2T_x$ films annealed at various temperature; the thickness dependence at the annealing temperature of 350°C is shown in fig. S16. To gain further insight, the increments in SE_T, SE_R, and SE_A values are shown in Fig. 2C as ΔSE_T, ΔSE_R, and ΔSE_A, respectively, as a function of annealing temperature. ΔSE represents the extent of SE increase after annealing compared with the as-synthesized materials. The SE_T and SE_A of Ti_3CNT_x films rapidly increase with increasing annealing temperature, whereas the SE_R values are almost independent of annealing temperature. $Ti_3C_2T_x$ films also reveal the same trend as Ti_3CNT_x films. However, the increment rate in $Ti_3C_2T_x$ is much smaller than that in Ti_3CNT_x at the same annealing conditions. ΔSE_T values for pristine and annealed films of 40-μm thickness after annealing at 350°C reach 55 dB for Ti_3CNT_x and 9 dB for $Ti_3C_2T_x$, which are equivalent to a 90% and 12.6% improvement in SE_T compared with the as-synthesized materials, respectively. The temperature dependence of ΔSE for the samples with different thicknesses (10, 20, and 30 μm in fig. S17) follow the same trend shown in Fig. 2C for both the MXenes. EMI ΔSE values for Ti_3CNT_x and $Ti_3C_2T_x$ annealed at 350°C are presented

as a function of thickness in Fig. 2D. At the same annealing temperature, as the sample thickness increases from 10 to 40 μm, ΔSE_T increases substantially, from 31.6 to 54.7 dB, for Ti_3CNT_x and just slightly, from 6.0 to 8.6 dB, for $Ti_3C_2T_x$. The difference between the ΔSE_T of Ti_3CNT_x and $Ti_3C_2T_x$ films becomes larger with increasing sample thickness. As a result, even though the as-synthesized Ti_3CNT_x films always have smaller SE_T and SE_A values than the as-synthesized $Ti_3C_2T_x$ films, the annealed Ti_3CNT_x films have larger SE_T and SE_A values than the annealed $Ti_3C_2T_x$ films. The enhancement in SE_T and ΔSE_T of Ti_3CNT_x films after annealing or in thicker samples is solely contributed by the SE_A and ΔSE_A because the SE_R values are almost independent of the annealing temperature.

Annealing time also strongly influences the structure and shielding performance of Ti_3CNT_x films. After annealing for 1 hour at 350°C, the electrical conductivity of the Ti_3CNT_x film increases from 1125 to 2520 S cm^{-1}, and then gradually decreases with time to 512 S cm^{-1} after 24 hours (Fig. 2E) because of excessive oxidation (fig. S18A). EMI SE of Ti_3CNT_x films also shows a similar trend. However, moderate oxidation after 6 hours of annealing, setting the electrical conductivity value to 1786 S cm^{-1}, resulted in the highest EMI SE of 116 dB (Fig. 2E and fig. S19), confirming once again that for 2D materials there is not a monotonous increase of EMI SE with conductivity. With the saturated pore volume in all samples treated at 350°C for a range of annealing times (fig. S18B), all the annealed films show similar SE_R values (fig. S19B); however, SE_A significantly increases with the annealing time up to 6 hours (fig. S19C), indicating an anomalously large improvement in absorption of electromagnetic (EM) waves.

This substantial increase in SE_A can partially be attributed to the improved electrical conductivity, the induced porosity, and dipolar polarizations in the annealed Ti_3CNT_x laminate films. The SE_A is proportional to the electrical conductivity, which is responsible for the rapid exponential decay in the strength of incoming EM waves in the form of heat caused by ohmic and eddy current losses (see Eq. 9 in the supplementary materials) (*25*, *26*). The porous structure provides extra interfaces for internal reflections that extend the path length of the EM wave during propagation in the film before transmission, and the wave interacts with each interface, resulting in extra attenuation by absorption (see Eqs. 12 to 14 in the supplementary materials) (*12*, *15*). The remaining surface terminations and formation of dielectric TiO_2 on the surface of Ti_3CNT_x may also contribute to the enhanced absorption of EM waves by generating dipole polarization losses within the shield (*20*). By contrast, the reflection contribution (SE_R) depends on the logarithm of electrical conductivity (see Eq. 8 in the supplementary materials), which in this case would change marginally. Therefore, the SE_R values of both Ti_3CNT_x and $Ti_3C_2T_x$ show a negligible change after annealing.

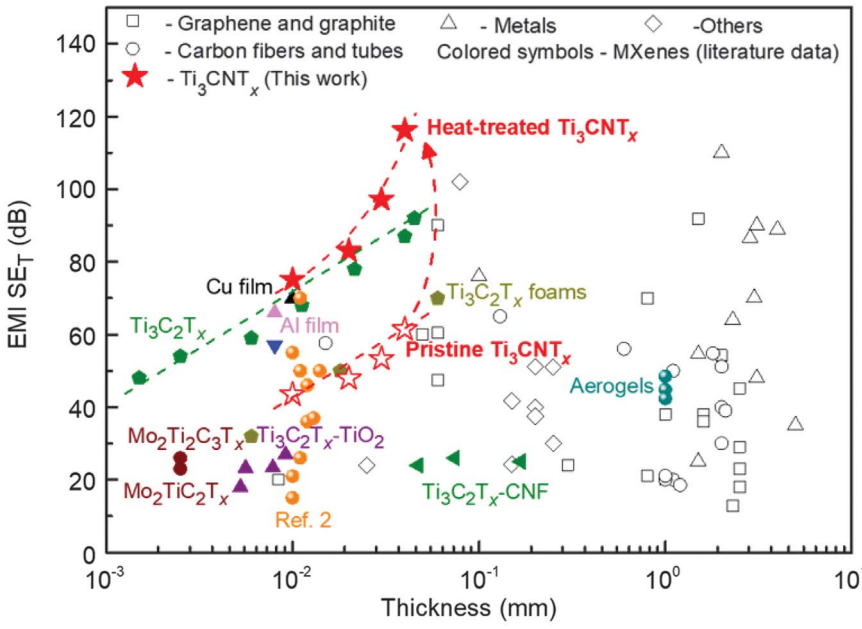

Fig. 3. Comparison of EMI SE_T of reported shielding materials. EMI SE_T versus thickness of annealed Ti_3CNT_x films and materials reported in the literature. At the comparable thickness, our annealed Ti_3CNT_x MXene lies above these materials.

The Ti_3CNT_x film annealed at 350°C has much larger EMI SE_A and SE_T than the one annealed at 250°C, despite its lower electrical conductivity. Moreover, the Ti_3CNT_x film annealed at 350°C has much larger SE_A and SE_T than the $Ti_3C_2T_x$ annealed at the same temperature, which has a much higher electrical conductivity. Our results suggest a possible role of the induced porous structure coupled with partial oxidation in enhancing the electromagnetic absorption. However, still lacking is a fundamental understanding of the interaction of electromagnetic waves with nanometer-thin 2D metals such as MXenes, where macroscopic theories cannot be used and a quantum mechanical approach is required.

The experimental SE_T, SE_R, and SE_A results for Ti_3CNT_x and $Ti_3C_2T_x$ laminate films were compared with the theoretical calculations obtained with the transfer matrix method (see fig. S20; for more details, see the supplementary materials) (*27*, *28*) to investigate the effect of porosity (Fig. 2F and figs. S21 and S22). In the experimental data, each data point represents a different annealing temperature. The calculations assume that MXene films have the perfect laminate structure of 2D MXene sheets with infinite sheet area, and we simultaneously considered the effect of conductivity and porosity. The calculations show that as the conductivity and porosity increase, SE_T and SE_A increase separately, but SE_R varies only slightly. The experimental SE_T value of the as-synthesized Ti_3CNT_x without heat treatment qualitatively agrees with the theoretical value, in the same way as SE_T, SE_R, and SE_A of the as-synthesized and heat-treated $Ti_3C_2T_x$ films. However, after annealing, a mismatch between the experimental and theoretical SE_T values of Ti_3CNT_x MXene occurs and becomes more pronounced as the annealing temperature increases. Similarly, SE_A values also show a considerable mismatch between experimental and theoretical values at higher annealing temperatures, whereas all the experimental SE_R values are consistent with the theoretical calculations. This indicates that the mismatch in SE_T is because of the mismatch in SE_A, which originates from the unexpectedly large improvement in electromagnetic absorption after annealing. This again stresses the limitations of traditional models and the need for atomistic simulations.

The failure to theoretically predict the EMI shielding behavior of the annealed Ti_3CNT_x films indicates that, in addition to electrical conductivity and induced porosity, dipolar polarization and the low dimensionality of MXene should be considered. In particular, the extraordinarily large absorption of the annealed Ti_3CNT_x films may be caused by the formation of metamaterial-like structure from atomically thin MXene sheets after annealing (*29*, *30*). The increasing loss components of metamaterial's effective electric permittivity and magnetic permeability enhance absorption of electromagnetic radiation (30). Therefore,

further studies are needed to understand the particular shielding mechanism of Ti_3CNT_x that is responsible for the experimentally observed large absorption ability of the annealed Ti_3CNT_x samples.

The EMI SE_T of Ti_3CNT_x films is compared with the values reported in previous studies in Fig. 3 (details are provided in table S1). Metal-based and carbon-based materials have been on the forefront in the last decade, where SE in excess of 50 dB for a thickness between 50 and 100 μm has been considered sufficient for practical applications. However, the high density and difficult processing of metals into thin films limit their applications for advanced mobile applications. Carbon-based materials with lower electrical conductivity can only provide sufficient EMI SE at the expense of thickness. A thermally treated, 40-μm-thick Ti_3CNT_x MXene film exhibits an absorption-dominant EMI SE of 116 dB, showing its strong potential for EMI shielding and related applications.

In summary, the transition metal carbonitride Ti_3CNT_x MXene, with a relatively low electrical conductivity, exhibits outstanding electromagnetic absorption shielding ability after heat treatment at 350°C, resulting in better EMI shielding performance than highly conductive $Ti_3C_2T_x$ or metal foils of the same thickness. Heat treatment of Ti_3CNT_x improves electrical conductivity, removes molecular species adsorbed between MXene sheets, and produces a porous architecture, but these factors alone do not fully explain the observed increase within the framework of existing shielding theories. Our findings show the need for further exploration of the fundamental mechanisms behind the interaction of electromagnetic waves with 2D nanostructures.

REFERENCES AND NOTES

1. F. Shahzad *et al*., *Science* **353**, 1137–1140 (2016).
2. M. Han *et al*., *ACS Nano* **14**, 5008–5016 (2020).
3. B. Shen, W. Zhai, W. Zheng, *Adv. Funct. Mater.* **24**, 4542–4548 (2014).
4. W. T. Cao *et al*., *ACS Nano* **12**, 4583–4593 (2018).
5. G.-M. Weng *et al*., *Adv. Funct. Mater.* **28**, 1803360 (2018).
6. Z. Chen, C. Xu, C. Ma, W. Ren, H.-M. Cheng, *Adv. Mater.* **25**, 1296–1300 (2013).
7. T. Yun *et al*., *Adv. Mater.* **32**, e1906769 (2020).
8. M. H. Al-Saleh, W. H. Saadeh, U. Sundararaj, *Carbon* **60**, 146–156 (2013).
9. N. Li *et al*., *Nano Lett.* **6**, 1141–1145 (2006).
10. M.-S. Cao, X.-X. Wang, W.-Q. Cao, J. Yuan, *J. Mater. Chem. C Mater. Opt. Electron. Devices* **3**, 6589–6599 (2015).
11. Z. Li, Z. Wang, W. Lu, B. Hou, *Metals (Basel)* **8**, 652 (2018).
12. J. Liu *et al*., *Adv. Mater.* **29**, 1702367 (2017).
13. R. Sun *et al*., *Adv. Funct. Mater.* **27**, 1702807 (2017).
14. M. Han *et al*., *Adv. Opt. Mater.* **7**, 1900267 (2019).
15. P. Sambyal *et al*., *ACS Appl. Mater. Interfaces* **11**, 38046–38054 (2019).
16. K. Hantanasirisakul, Y. Gogotsi, *Adv. Mater.* **30**, e1804779 (2018).
17. K. Hantanasirisakul *et al*., *Chem. Mater.* **31**, 2941–2951 (2019).
18. M. Radovic, A. Ganguly, M. W. Barsoum, *J. Mater. Res.* **23**, 1517–1521 (2008).
19. M. Naguib *et al*., *Adv. Mater.* **23**, 4248–4253 (2011).
20. M. Han *et al*., *ACS Appl. Mater. Interfaces* **8**, 21011–21019 (2016).
21. R. P. Pandey *et al*., *J. Mater. Chem. A Mater. Energy Sustain.* **6**, 3522–3533 (2018).
22. S. J. Kim *et al*., *ACS Nano* **12**, 986–993 (2018).
23. J. L. Hart *et al*., *Nat. Commun.* **10**, 522 (2019).
24. G. Liu *et al*., *Nanotechnology* **23**, 294003 (2012).
25. Y. Xu, Y. Li, W. Hua, A. Zhang, J. Bao, *ACS Appl. Mater. Interfaces* **8**, 24131–24142 (2016).
26. T. Habib *et al*., *Sci. Rep.* **9**, 16489 (2019).
27. R. Moore, *Electromagnetic Composites Handbook* (McGraw-Hill Education, ed. 2, 2016).
28. M. Born, E. Wolf, A. B. Bhatia, *Principles of Optics: Electromagnetic Theory of Propagation, Interference and Diffraction of Light* (Cambridge Univ. Press, 2016).
29. R. S. Kshetrimayum, *IEEE Potentials* **23**, 44–46 (2005).
30. N. I. Landy, S. Sajuyigbe, J. J. Mock, D. R. Smith, W. J. Padilla, *Phys. Rev. Lett.* **100**, 207402 (2008).

ACKNOWLEDGMENTS

We thank B. Anasori (Purdue School of Engineering and Technology, Indiana University – Purdue University Indianapolis) and M. Alhabeb (Drexel University) for providing the Ti_3AlCN MAX powder for this study. We also thank Y. S. Cho for preparing TEM samples, Y. Kim for assisting in theoretical calculations, and S. M. Hong and S. J. Kim for helpful discussion and comments. **Funding:** This work was supported by a grant from the Construction Technology Research Project (19SCIP-B146646-02), funded by the Ministry of Land, Infrastructure, and Transport; the Basic Science Research Program (2017R1A2B3006469) through the National Research Foundation of Korea, funded by the Ministry of Science, ICT, and Future Planning; the Fundamental R&D Program (10077545) for Core Technology of Materials; the Industrial Strategic Technology Development Program, funded by the Ministry of Trade, Industry, and Energy, Republic of Korea. This work was also financially supported by KU-KIST Research, Young Fellow, and KIST School Partnership Project and KIST Internal Research programs, funded by the Korea Institute of Science and Technology (KIST). This work was technically supported by Pohang Light Source. Development of characterization of Ti_3CNT_x MXene by Y.G. and K.H was supported by the U.S. Department of Energy (DOE), Office of Science, Office of Basic Energy Sciences (grant no. DESC0018618). **Author contributions:** A.I. and C.M.K. conceived the idea. A.I. performed the experiments for this study under the guidance of C.M.K. and Y.G. K.H. performed TGA-MS and XPS analysis. H.K. and D.K. helped with MXene synthesis. J.H. helped with EMI shielding measurements. M.-K.K., J.K., and C.M.K. conducted theoretical calculations. All authors contributed to the interpretation of the results and gave valuable suggestions. A.I., F.S., and C.M.K. drafted the manuscript. Y.G. reviewed and edited the manuscript. C.M.K. and Y.G. supervised the whole project. **Competing interests:** Y.G. is also affiliated with the Korea Advanced Institute of Science and Technology (KAIST), Republic of Korea, and Shinshu University, Japan. A.I., K.H., Y.G., and C.M.K. are coinventors on U.S. patent application 62/979,365 that covers transition metal carbonitride MXene films for EMI shielding. **Data and materials availability:** All data corresponding to this study are available in the main text and the supplementary materials.

SUPPLEMENTARY MATERIALS

science.sciencemag.org/content/369/6502/446/suppl/DC1
Materials and Methods
Supplementary Text
Figs. S1 to S22
Table S1
References (*31*–*75*)

7 January 2020; accepted 5 June 2020
10.1126/science.aba7977